

# Constraining the mass distribution of galaxies using galaxy-galaxy lensing in clusters and in the field

Marceau Limousin,<sup>1</sup> Jean-Paul Kneib<sup>1,2</sup> & Priyamvada Natarajan<sup>3</sup>

<sup>1</sup> *Observatoire Midi-Pyrénées, UMR5572, 14 Avenue Edouard Belin, 31400 Toulouse, France.*

<sup>2</sup> *Caltech, Astronomy, MC105-24, Pasadena, CA 91125, USA.*

<sup>3</sup> *Dept. of Astronomy, Yale University, P.O. Box 208101, New Haven, CT 06250, USA.*

## ABSTRACT

We present a maximum-likelihood analysis of galaxy-galaxy lensing effects in galaxy clusters and in the field. The aim is to determine the accuracy and robustness of constraints that can be obtained on galaxy halo properties in both environments - the high density cluster and the low density field. This paper is theoretically motivated, therefore, we work exclusively with simulated data (nevertheless defined to match observations) to study the accuracy with which input parameters for mass distributions for galaxies can be extracted. We model galaxies in the cluster and the field using a wide range of mass profiles: the truncated pseudo isothermal elliptical mass distribution, the Navarro, Frenk and White profile, and a Power Law model with a core radius. We find that independent of the choice of profile the mean mass of galaxies (of the order of  $10^{12} M_{\odot}$ ) can be estimated to within 15% from ground-based data and with an error of less than 10% with space observations. Additionally robust constraints can be obtained on the mean slope of the mass profile. The two standard parameters that characterise galaxy halo models, the central velocity dispersion and the truncation radius can also be retrieved reliably from the maximum-likelihood analysis. We find that there is an optimal scale  $R_{\max}$  which marks the boundary between lenses that effectively contribute to the measured shear. Lenses beyond  $R_{\max}$  in fact dilute the shear signal. Furthermore, going beyond the usual formulation, we propose a re-parameterisation of the mass models that allows us to put yet stronger constraints on the aperture mass of a galaxy halo (with less than 10% error). The gain in signal to noise using space observations, expected for instance with the proposed SNAP satellite compared to ground based data in terms of accuracy of retrieving input parameters is highly significant.

**Key words:** Galaxies, Dark Matter Halos, Cosmology, Lensing.

## 1 INTRODUCTION

Gravitational lensing has now become a popular tool to measure the mass distribution of structure in the Universe on a range of scales. Recently, there has been considerable progress in mapping the mass distribution on relatively large scales using cosmic shear (Refregier et al. 2003), and on cluster scales combining strong and weak lensing features (Gavazzi et al. 2003; Kneib et al. 2003). On the scale of individual galaxies as well, there has been much work done on modeling and understanding multiple quasar systems (Fassnacht et al. 1999; Phillips et al. 2004). In fact, in many cases it has become clear that it is almost never a unique lens that is responsible for the detected lensing and the presence of a nearby galaxy, group or cluster along the line of sight plays an important role in inducing the shear and amplification (Keeton, Kochanek, & Seljak 1997; Kneib

2000; Möller et al. 2002). In other words, there are likely no clean lines of sight and comprehensive modeling is needed to map the lensing configuration accurately. Therefore the mass mapping problem is best tackled using an “inverse” approach where the adopted method is to model the distribution of matter around many lines of sight, and optimise the mass distribution to match the observations as closely as possible.

Analysing galaxy-galaxy lensing using maximum-likelihood lensing techniques is an example of such a method. Indeed, the goal of galaxy-galaxy lensing is to obtain constraints on the physical parameters that characterise the dark matter halos of galaxies. This is accomplished directly using lensing since the deformation in the shapes of background galaxies produced by the foreground lenses although weak is observationally detected statistically. The difficulty is that multiple deflections frequently occur along the line

arXiv:astro-ph/0405607v1 30 May 2004

of sight, and therefore, nearby groups or clusters can have an important effect yet again on the resultant distortions. This introduces a systematic bias in the mass obtained for the deflectors when using simple models.

Galaxy-galaxy lensing work began with the first detection of the signal from ground based data (Brainerd, Blandford & Smail 1996, hereafter BBS) and later with the *Hubble Space Telescope* (HST) data (Griffiths et al. 1996). Maximum-likelihood techniques have been developed by Schneider & Rix (1997), Natarajan & Kneib (1997) and Geiger & Schneider (1998) to obtain constraints on galaxy halo properties in clusters and in the field. The results of these analyses suggest that galaxy halos in clusters are significantly less massive but more compact compared to galaxy halos around field galaxies of equivalent luminosity (Natarajan 1998, Natarajan 2002a). Besides, in the case of galaxy halos in the field no clear edge is detected to the mass distribution even on scales of the order of a few hundred kpc (McKay et al. 2001; Fisher et al. 2000). Only two published studies to date by Hoekstra (2003); Hoekstra, Yee & Gladders (2004) have been able to put an upper bound on the characteristic extension of a field halo at about  $290_{-82}^{+139} h^{-1}$  kpc and  $185_{-28}^{+30} h^{-1}$  kpc, which are only marginally consistent with each other. Besides these large values do not impose a stringent constraint for typical galaxy mass distributions since at these typical radii the galaxy density is only a few times above the mean density of the Universe.

Galaxy-galaxy lensing studies provide information on average properties of the halo population, therefore the results depend on the specific parameterised model chosen to fit the observational data. From a purely observational point of view, the reliability of the galaxy-galaxy lensing signal depends on the number density of galaxies whose distorted shapes can be reliably measured, as well as any additional constraints that can be added to the analysis, for instance, redshifts of the lens galaxies, redshifts of the source galaxies, galaxy type, dynamical constraints, and the presence of larger scale structure like groups or clusters in the vicinity.

Other methods to determine the masses of galaxies are generally based on the dynamical properties of the luminous matter: measurement of the rotation curve or velocity dispersion, study of the velocity field of nearby objects like planetary nebulae, globular clusters, and satellite galaxies. These dynamical methods are complementary to lensing, but often probe much smaller scales. The study of the velocity field around galaxies for instance, is generally limited to local galaxies, however with the large spectroscopic surveys such as 2dF and SDSS, it is now possible to extend such analyses to larger scales (Prada et al. 2003; Brainerd & Specian 2003). Probing the dynamics of stars in galaxies is limited to the inner regions when studying high redshift galaxies. Therefore, at the present time there is limited direct overlap between lensing and dynamical studies in terms of scales probed. Although this situation is likely to change in the very near future when large spectroscopic surveys of distant galaxies such as the DEEP2 survey (Davis et al. 2003), the VVDS survey (Le Fevre et al. 2003) or the z-COSMOS survey (<http://webast.ast.obs-mip.fr/zCosmos>) are completed.

The inner slopes of density profiles provide a strong test of structure formation in cold dark matter models and lensing provides an unbiased way to estimate the slopes. Treu & Koopmans (2004) and Koopmans & Treu (2003)

have studied the slope of the mass distribution at small radii (on scales ranging from a few to about 20 kpc) by combining dynamical estimates and strong lensing constraints. They find that the mass distribution profile is flatter than the singular isothermal sphere (SIS) profile but steeper than the NFW profile. Therefore, there is mounting evidence for the lack of cores (a constant density region) in galaxies as well as in clusters.

The galaxy-galaxy lensing results from the Sloan Digital Sky Survey have also provided (McKay et al. 2001; Sheldon et al. 2003) interesting constraints on the distribution of light and dark matter in galaxies. Mass and light trace seem to trace each other reasonably well. The power of galaxy-galaxy lensing is that it provides a probe of the gravitational potential of the halos of galaxies out to large radii, where no other methods are viable for inter-mediate as well as high redshift galaxies independent of the dynamical state of the system. A similar approach combining dynamical estimates of the central part of galaxies and galaxy-galaxy lensing is planned in the future as part of the GEMS and COSMOS projects.

This paper is organised as follows: in section 2, we describe the method adopted to model galaxy lenses, source galaxies, the simulations performed to recover the INPUT parameters of the lenses and the calculation of the aperture mass. In section 3, we present the results for three different classes of lens models considered in this work. In section 4, we explore the results of re-parameterising the models. Whenever necessary our results are scaled to the currently preferred flat, low matter density  $\Lambda$ CDM cosmology with  $\Omega_M = 0.3$ ,  $\Omega_\Lambda = 0.7$  and a Hubble constant  $H_0 = 65 h_{65}$   $\text{kms}^{-1} \text{Mpc}^{-1}$ . In such a cosmology, at  $z = 0.2$ ,  $1''$  corresponds to  $3.55 h_{65}^{-1}$  kpc.

## 2 GALAXY-GALAXY LENSING

We briefly review the basic principles of gravitational lensing of distant galaxies before describing the mass distributions adopted to model them. This section concludes with the presentation of our method to recover the lensing galaxy parameters.

### 2.1 Lensing equation

The light rays emitted by a distant galaxy are distorted en-route to us by the presence of mass concentrations along the line of sight. The distortion can produce strong effects like multiple images or arcs if there is close alignment between the distant source and a foreground source, but most of the time only a weak distortion occurs in the galaxy shape.

Let us consider the multiple lensing equation (Schneider et al. 1992). For two lenses A and B, the lens equation becomes:

$$\vec{\beta} = \vec{\theta} - \vec{\alpha}_A \frac{D_{AS}}{D_{OS}} - \vec{\alpha}_B \frac{D_{BS}}{D_{OS}} \quad (1)$$

where  $\vec{\beta}$  is the source position,  $\vec{\alpha}_A$  is the deflection due to the lens A,  $\vec{\alpha}_B$  is the deflection due to the lens B and  $D_{AS}$ ,  $D_{BS}$  and  $D_{OS}$  are the angular diameter distances between source plane S and lens A, lens B and the observer respectively (note that we must have  $z_A < z_B < z_S$ ). The deflection

angle  $\vec{\alpha}_X$  due to the lens  $X$  is proportional to the angular distance  $D_{OX}$  between observer and lens  $X$  and to the gradient of the projected gravitational potential  $\phi$  generated by the lens  $X$ .

For a given background galaxy (i) and its associated lens (j), we can construct the amplification matrix  $a_{ij}$ , which provides the mapping between the source plane and the image plane:

$$a_{ij} = \begin{pmatrix} 1 - \kappa^{ij} - \gamma_1^{ij} & -\gamma_2^{ij} \\ -\gamma_2^{ij} & 1 - \kappa^{ij} + \gamma_1^{ij} \end{pmatrix} \quad (2)$$

where  $\kappa$  is the convergence, and  $\gamma_1, \gamma_2$  are the two components of the shear. In the case of multiple deflections (more than one lens contributing to the observed distortion), we will assume that the total amplification matrix  $a_i$  of the distant galaxy (i) is equal to the sum of the individual contributions  $a_{ij}$  from to each lens:

$$a_i = \sum_j a_{ij} \quad (3)$$

This assumption relies on the fact that we are in the weak lensing regime and that the distance between the lenses is large compared to the Einstein radius of each individual lens. For instance, in the simulations performed in this paper, the separation between two lenses is larger than  $3''$ , when a typical value for the Einstein radius is about  $1''$ .

## 2.2 Modeling the mass distribution of galaxies

Lensing probes the two dimensional projected mass along the line of sight, therefore, we deal with the two dimensional potential,  $\phi(R)$ , resulting from the three dimensional density distribution  $\rho(r)$  projected onto the lens plane. The related projected surface mass density  $\Sigma$  is then given by:

$$4\pi G\Sigma(R) = \nabla^2 \phi(R) \quad (4)$$

Moreover, we are interested in the two-dimensional projected mass inside radius  $R$  (the aperture radius  $R_{aper}$ ) defined as follows:

$$M_{aper}(R) = 2\pi \int_0^R \Sigma(r)rdr \quad (5)$$

In this paper, we study three different mass models (i) the two component pseudo-isothermal mass distribution (*PIEMD*) (Kneib 1996), which is a more physically motivated mass profile than the isothermal sphere profile (*SIS*) but sharing the same profile slope at intermediate radius; (ii) the *NFW* (Navarro, Frenk & White 1997) profile and (iii) a Power Law profile with core radius (*PL*). These enable us to explore a wide range of mass distributions and reveal the important parameters that lensing is sensitive to.

### 2.2.1 PIEMD profile

The density distribution for this model is given by:

$$\rho(r) = \frac{\rho_0}{(1 + r^2/r_{core}^2)(1 + r^2/r_{cut}^2)} \quad (6)$$

with the core radius  $r_{core}$  of the order of 100 pc, and a truncation radius  $r_{cut}$ . We also introduce a shape parameter  $a = r_{cut}/r_{core}$ . In the centre,  $\rho \simeq \rho_0/(1+r^2/r_{core}^2)$  which

describes a core with central density  $\rho_0$ . The transition region ( $r_{core} < r < r_{cut}$ ) is isothermal, with  $\rho \simeq r^{-2}$ . In the outer parts, the density falls off as  $\rho \simeq r^{-4}$ , as is usually required for models of elliptical galaxies. Fig. 1 illustrates this behaviour. These models have been successfully used by Natarajan et al. (1998, 2002) to fit observed early-type galaxies in cluster lenses.

Integrating equation 6, we obtain the 2 dimensional surface mass density distribution:

$$\Sigma(R) = \frac{\sigma_0^2 r_{cut}}{2G(r_{cut} - r_{core})} \left( \frac{1}{\sqrt{r_{core}^2 + R^2}} - \frac{1}{\sqrt{r_{cut}^2 + R^2}} \right) \quad (7)$$

where  $\sigma_0$  is the central velocity dispersion for a circular potential related to  $\rho_0$  by the following relation:

$$\rho_0 = \frac{\sigma_0^2}{2\pi G} \left( \frac{r_{cut} + r_{core}}{r_{core}^2 r_{cut}} \right) \quad (8)$$

It can be shown that for a vanishing core radius, the surface mass profile obtained above becomes identical to the surface mass profile used by BBS for modeling galaxy-galaxy lensing. The enclosed two dimensional aperture mass interior to radius  $R$  is:

$$M_{aper}(R) = \frac{\pi r_{cut} \sigma_0^2}{G} \left( 1 - \frac{\sqrt{r_{cut}^2 + R^2} - \sqrt{r_{core}^2 + R^2}}{r_{cut} - r_{core}} \right) \quad (9)$$

and the total mass of such a model is finite and is given by:

$$M_{tot} = \frac{\pi \sigma_0^2}{G} \frac{r_{cut}^2}{r_{cut} + r_{core}} \simeq \frac{\pi \sigma_0^2 r_{cut}}{G} \quad (10)$$

Fig. 1 shows the behaviour of  $M_{aper}$  as a function of the aperture radius  $R_{aper}$  and of  $\rho(r)$  for such a profile, with  $\sigma_0 = 220 \text{ kms}^{-1}$ ,  $r_{core} = 0.1''$ ,  $r_{cut} = 30''$ .  $\rho(r)$  is also shown, normalised to the critical density of the Universe  $\rho_{crit}$ , where  $\rho_{crit} = 3H_0^2/8\pi G$ .

### 2.2.2 NFW profile

The NFW density profile (Navarro, Frenk & White 1997) provides the best-fit to the halos that form in N-body simulations of collisionless dark matter. In fact the NFW profile reproduces with good accuracy the radial distribution of structures in these simulations over 9 orders of magnitude in mass (from the scale of globular clusters to that of massive galaxy clusters). Since it is thought that matter in the Universe is dominated by a form of dissipationless cold dark matter, this ‘‘universal profile’’ offers an interesting and natural way of describing mass concentrations. The density distribution of the NFW profile is given by:

$$\rho(r) = \frac{\rho_s}{(r/r_s)(1 + r/r_s)^2} \quad (11)$$

where  $\rho_s$  is a characteristic density. It is possible to parameterise this model in terms of  $M_{200}$ , which is the mass contained in a radius  $r_{200}$  where the criterion  $\bar{\rho} = 200\rho_{crit}$  holds, and  $\delta_c$  the density contrast (or equivalently  $c = r_{200}/r_s$ , the concentration parameter). We have the following relations between the two parameterisations:

$$\rho_s = \delta_c \rho_c, \quad M_{200} = \frac{800}{3} \pi r_{200}^3 \rho_c, \quad \delta_c = \frac{200}{3} \frac{c^3}{\ln(1+c) - \frac{c}{1+c}} \quad (12)$$

The properties of the projected quantities depends on the ratio  $r/r_s$ , so it is useful to introduce the dimensionless radial coordinate,  $x = r/r_s = R/r_s$ . Moreover, the velocity dispersion  $\sigma(r)$  of this potential, computed with the Jeans equation assuming an isotropic velocity distribution, gives an unrealistic central velocity dispersion ( $\sigma(0) = 0$ ). In order to compare the NFW potential with other potentials used to model lenses, we define a characteristic velocity  $\sigma_s$  as follows:

$$\sigma_s^2 = \frac{4}{3} G r_s^2 \rho_s \quad (13)$$

The surface mass density for the NFW is given by:

$$\Sigma(x) = \int_{-\infty}^{+\infty} \rho(r_s, x, z) dz = 2\rho_s r_s F(x) \quad (14)$$

with

$$F(x) = \begin{cases} \frac{1}{x^2-1} \left(1 - \frac{1}{\sqrt{1-x^2}} \operatorname{arctanh} \frac{1}{x}\right) & (x < 1) \\ \frac{1}{3} & (x = 1) \\ \frac{1}{x^2-1} \left(1 - \frac{1}{\sqrt{x^2-1}} \arccos \frac{1}{x}\right) & (x > 1) \end{cases} \quad (15)$$

and the two dimensional aperture mass  $M_{\text{aper}}$  contained within the dimensionless radius  $x$  is (Bartelmann 1996):

$$M_{\text{aper}}(R) = \frac{3\pi\sigma_s^2 r_s}{2G} g(x) \quad (16)$$

with

$$g(x) = \begin{cases} \ln \frac{x}{2} + \frac{1}{\sqrt{1-x^2}} \operatorname{arctanh} \frac{1}{x} & (x < 1) \\ 1 + \ln \left(\frac{1}{2}\right) & (x = 1) \\ \ln \frac{x}{2} + \frac{1}{\sqrt{x^2-1}} \arccos \frac{1}{x} & (x > 1) \end{cases} \quad (17)$$

and the mass  $M_{200}$  can be written as a function of  $\sigma_s$ ,  $r_{200}$  and  $c$ :

$$M_{200} = 200\pi \frac{c^2 \sigma_s^2 r_{200}}{\delta_c G} \quad (18)$$

Fig. 1 shows the behaviour of  $M_{\text{aper}}$  as a function of the aperture radius  $R_{\text{aper}}$  and of  $\rho(r)$ , with  $\sigma_s = 225 \text{ km s}^{-1}$  and  $r_s = 3''$ . This profile has a concentration parameter  $c = r_{200}/r_s \simeq 12$ , a typical value for a galaxy, and a projected mass inside  $r_{200}$ :  $M_{200}$  of  $\sim 3 \times 10^{12} M_{\odot}$ .

### 2.2.3 Power Law profile with a core

Another simple model to describe the mass distribution of a galaxy is a power-law model (PL) with a core. In a CDM dominated hierarchical structure formation scenario, mass profiles are expected to be independent of the mass scale, therefore a power-law profile is of interest. The PL mass distribution has three parameters: a core radius  $r_{\text{core}}$  of the order a kpc for an average galaxy, a central velocity dispersion,  $\sigma_0$  measured in ( $\text{km s}^{-1}$ ) and an exponent ( $\alpha$ ) which defines the gradient of the mass distribution. The three-dimensional density profile is (Kneib 1993):

$$\rho(r) = \rho_0 \frac{1 + \frac{1-2\alpha}{3} \left(\frac{r}{r_{\text{core}}}\right)^2}{\left(1 + \left(\frac{r}{r_{\text{core}}}\right)^2\right)^{2+\alpha}} \quad (19)$$

Introducing  $x = \frac{r}{r_{\text{core}}}$ , the density profile falls off as  $\rho \simeq x^{-2(1+\alpha)}$ . Note that the case  $\alpha=0$  corresponds to an isothermal sphere with a core radius, and  $\alpha > 0$  defines density profiles steeper than an isothermal sphere with a core radius. The relation between  $\rho_0$  and  $\sigma_0$  is given by:

$$\rho_0 = \frac{\sigma_0^2}{r_{\text{core}}^2} \frac{9(1-2\alpha)}{4\pi G} \quad (20)$$

The surface mass density is:

$$\Sigma(x) = \Sigma_0 \frac{1 + \frac{1-2\alpha}{2} x^2}{(1+x^2)^{3/2+\alpha}} \quad (21)$$

and the two dimensional aperture mass contained within the dimensionless radius  $x$  is:

$$M_{\text{aper}}(R) = \frac{3(1+2\alpha)\sigma_0^2 r_{\text{core}}}{G} \frac{x^2 + x^4}{(1+x^2)^{3/2+\alpha}} I_{1+\alpha} \quad (22)$$

with

$$I_{1+\alpha} = \int_0^{\infty} \frac{dx}{(1+x^2)^{1+\alpha}} \quad (23)$$

Fig. 1 shows the behaviour of  $\rho(r)$  and  $M_{\text{aper}}(r)$ , for such a profile, with  $\sigma = 400 \text{ km s}^{-1}$  and  $\alpha = 0.4$  (in this case,  $I_{1.4}=1.06$ ).

### 2.3 Comparing these profiles

Beginning with the Boltzmann equation to describe the behaviour of the cold dark matter collisionless particles that constitute a galaxy halo, the Jeans Equation for a spherical potential and for an isotropic velocity distribution ( $\sigma \equiv \sigma_r$ ) is given by:

$$\frac{1}{\rho} \frac{d(\sigma^2 \rho)}{dr} = -\frac{d\Phi}{dr} \quad (24)$$

where  $\Phi$  is the three dimensional potential. Considering the limit at  $+\infty$ , wherein  $\sigma(r) \rightarrow 0$  and  $\rho(r) \rightarrow 0$  to perform the integration, we have:

$$\sigma^2(r) = -\frac{1}{\rho(r)} \int_r^{+\infty} \rho(r') \frac{d\Phi(r')}{dr'} dr' \quad (25)$$

Solving this equation, does not lead generally to a simple analytical expression for the velocity dispersion.

Hence, one usually uses the rotation velocity defined as:

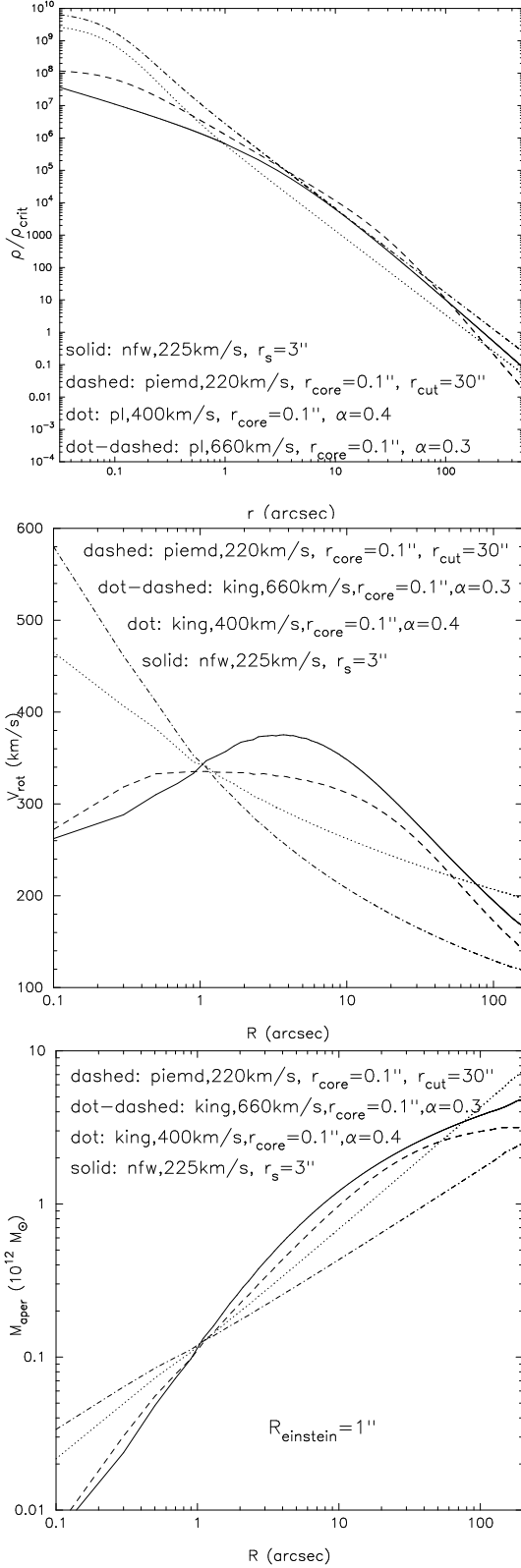
$$V_{\text{rot}}^2(R) = \frac{GM_{\text{aper}}(R)}{R} \quad (26)$$

Fig. 1 shows the behaviour of  $V_{\text{rot}}(R)$  for the three different mass profiles studied here.

It can be shown that for any spherically symmetric profile, the mass inside the Einstein radius  $R_E$  is proportional to  $R_E^2$ , so that profiles for which  $R_E$  is constant can be compared. It is easy to show (*e.g.* Kneib 1993) that:

$$M_{\text{aper}}(R_E) = \pi \Sigma_{\text{crit}} R_E^2 \quad (27)$$

Thus we adjust the parameters of the different mass profiles in order to have the same Einstein radius, and therefore the same mass within the Einstein radius. The results are illustrated in Fig. 2; this plot allows us to rescale the velocity dispersions derived for each profile. We can immediately see from this plot that for  $r > 4''$ , the shears computed from the three profiles are comparable. Note that in the case of the PL profile there is a strong dependence of the velocity dispersion on the value of the exponent  $\alpha$ . For example, the PL profile with  $\sigma_0 = 660 \text{ km s}^{-1}$  and an exponent of 0.3 induces the same shear as one with  $\sigma_0 = 400 \text{ km s}^{-1}$  and an exponent of 0.4. Therefore, there is degeneracy between the value of  $\sigma_0$  and  $\alpha$  for the PL profile. In order to illustrate



**Figure 1.** The density profile  $\rho(r)$ , the rotation velocity  $V_{\text{rot}}(R)$  and the aperture mass  $M_{\text{aper}}(R)$  for the 3 different mass profiles studied in this work. For each of these model profiles the relevant parameter choices are shown in the figure.

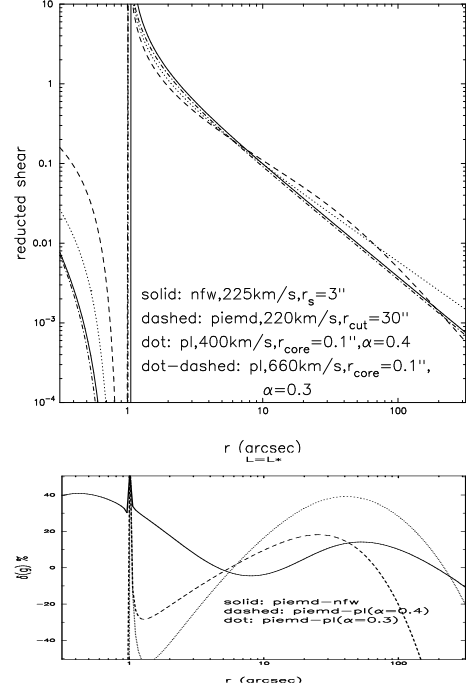


**Figure 2.** The reduced shears ( $\frac{\gamma}{1-\kappa}$ ) for the 3 different models for which the Einstein radius  $R_E = 1''$  (upper panel), and differences between them expressed as a percentage where we have used the PIEMD as the reference profile (lower panel).

the behaviour of the PL profile, we include this latter profile in Fig. 1 and 2.

### 3 SIMULATING GALAXY-GALAXY LENSING

#### 3.1 Measurement of background galaxy shapes

We study in detail the lensing effects in two observational scenarios: (i) a ground based survey using a wide field camera and (ii) data from space-based observations. Ground based data is characterised by the following image quality: seeing of about 0.6-0.8 arcsec, and a galaxy number density of 20-40 galaxies per square arcminute, of which only 50-70% can generally be used to measure their shapes reliably. The above estimates were obtained from two hours of observation in the R band with the CFH12k camera with a field of view of 44x28 square arcminutes.

Space observations have a significantly better image quality, with a PSF of about 0.1 to 0.15 arcsec, and a galaxy number density of about 40-100 galaxies per square arcminute (SNAP mission sensitivities - see Rhodes et al. (2003)), of which about 80% can be used in a weak lensing study since their shapes can be measured to the requisite degree of precision. Half an hour of observation in the R band of A2218 with the HST have provided the above estimates.

The measurement of shapes of lensed background galaxies is made using the second moment of the intensity of their light distribution. The quantity that is extracted for each galaxy is its complex ellipticity,  $e$  defined as  $e = \frac{e_1}{1} + ie_2$ . The magnitude of the ellipticity is  $e = \sqrt{e_1^2 + e_2^2}$ , the mean ellipticity  $m = \frac{\sum_i e_i}{N}$ , the dispersion of the elliptic-

ity is equal to the square root of the variance, defined by  $var = \frac{\sum_i (e_i - m)^2}{N}$ , where N is the number of objects.

### 3.2 Scaling the mass distribution from the light distribution

The foreground lenses are described by a mass profile with known input parameters. The parameters used to describe the different lenses are scaled as a function of luminosity. The scaling relation for  $\sigma_0$  assumes that mass traces light, and its origin resides in the Tully-Fisher or Faber-Jackson relations. The scaling relation for the radial parameter assumes that the mass-to-light ratio is constant for all galaxies. Note that they are other possible scaling relations, and that in principle we can test them with lensing.

#### 3.2.1 PIEMD profile

We have for this profile:

$$\sigma_0 = \sigma_0^* \left(\frac{L}{L^*}\right)^{\frac{1}{4}} \quad \& \quad r_{cut} = r_{cut}^* \left(\frac{L}{L^*}\right)^{\frac{1}{2}} \quad (28)$$

The parameter  $r_{core}$  is kept fixed at 0.1" - a fairly typical value for a galaxy.

From equation (13), we can scale the total mass with the luminosity as:

$$M_{tot} = \frac{\pi \sigma_0^2 r_{cut}}{G} = \frac{\pi \sigma_0^{*2} r_{cut}^*}{G} \left(\frac{L}{L^*}\right)^{3/4} \quad (29)$$

#### 3.2.2 NFW profile

Similar to the PIEMD profile, we have:

$$\sigma_0 = \sigma_0^* \left(\frac{L}{L^*}\right)^{\frac{1}{4}} \quad \& \quad r_s = r_s^* \left(\frac{L}{L^*}\right)^{\frac{1}{2}} \quad (30)$$

#### 3.2.3 PL profile

For the PL profile:

$$\sigma_0 = \sigma_0^* \left(\frac{L}{L^*}\right)^{\frac{1}{4}} \quad \& \quad r_{core} = r_{core}^* \left(\frac{L}{L^*}\right)^{\frac{1}{2}} \quad (31)$$

In order to illustrate the coherence of these scaling laws, we show the shear profiles obtained for a typical faint ( $L = L^*/10$ ) and bright ( $L = 3L^*$ ) galaxy (see Fig. 3).

### 3.3 Background galaxies

The way we simulate the background source population is the same for the 2 cases when the lenses belong to a cluster versus when they are field galaxies:

- they are allocated random positions
- number counts are generated in consonance with galaxy counts typical for a 2 hour integration time in the R-band. The magnitudes are assigned by drawing the number count observed with the *CFHT*
- the shapes are assigned by drawing the ellipticity from a gaussian distribution similar to the observed *CFHT* ellipticity distribution (see Fig. 4)

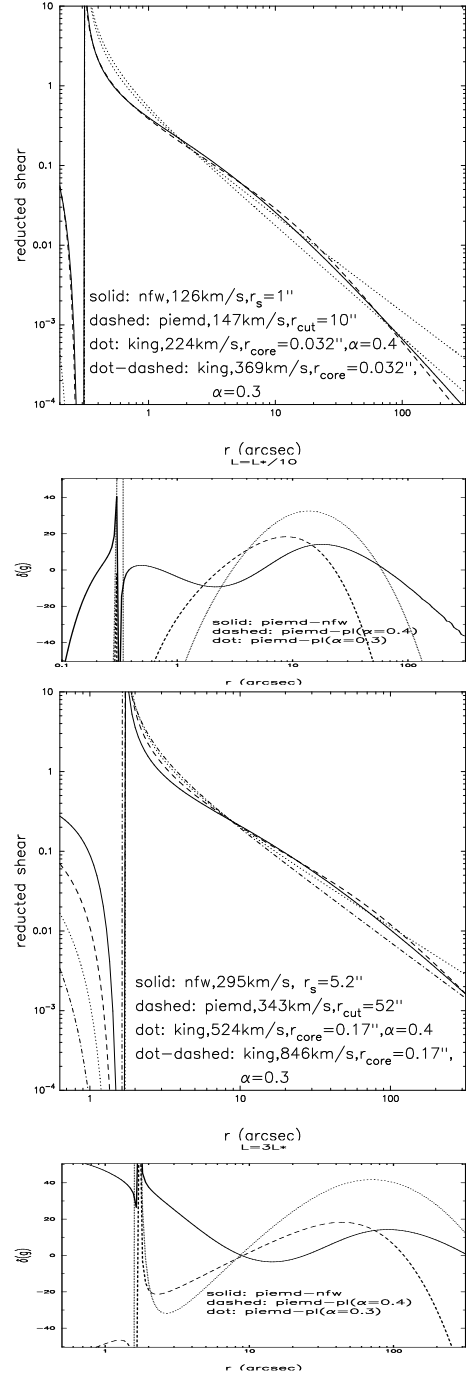


**Figure 3.** The reduced shears ( $\frac{\gamma}{1-\kappa}$ ) for each profile (Panels 1 and 3) and differences between them expressed in percentages (Panel 2 and 4), for  $L = L^*/10$  and  $L = 3L^*$  respectively, where once again the PIEMD is the reference profile.

- Redshift distribution: We use the R-band to define the number counts of galaxies and use the HDF prescription in terms of the mean redshift per magnitude bin, and the same redshift distribution as BBS.

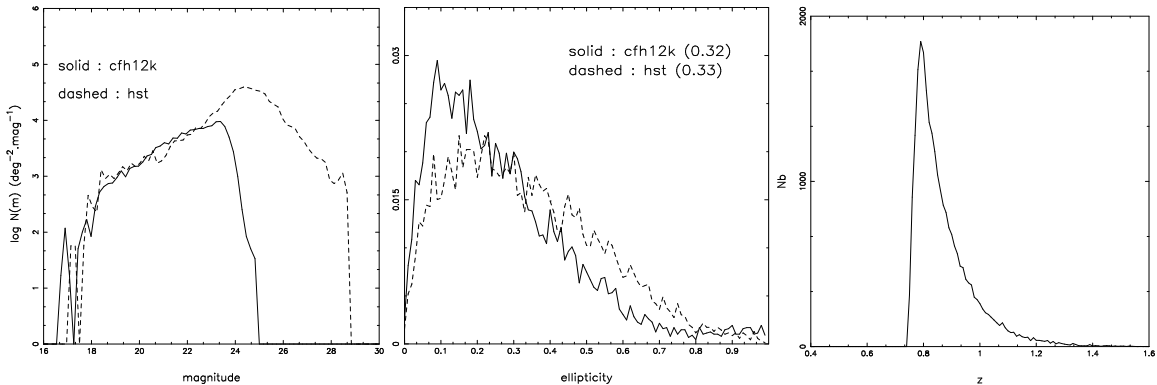


**Figure 4.** Galaxy counts from CFH12k and HST data (Left panel), and the ellipticity distributions for the CFH12k and HST data (Center panel). The value in parentheses is the mean value of the ellipticity in each case. Right panel: the redshift distribution of the background population in our simulations.

### 3.4 Lens galaxies

The way we simulate the foreground lenses galaxies is different in the case of galaxies inside the cluster and in the field.

#### 3.4.1 Cluster Galaxies

We put the individual lenses constituting a cluster at a redshift of 0.2, and model it as a superposition of large-scale smooth cluster component and a few clumps. In order to obtain a better match to the real data, the positions and the magnitudes of the foreground cluster galaxies are drawn from the positions and the magnitudes of ellipticals in the cluster A1689 at  $z = 0.18$ .

#### 3.4.2 Field Galaxies

For simplicity, the lenses are randomly distributed in position and uniformly distributed in a redshift range from 0.2 to 0.5. This distribution is a crude approximation of reality.

## 4 MAXIMUM LIKELIHOOD ANALYSIS

### 4.1 Methodology

Using the foreground cluster and field galaxies as the lens for the sheet of generated background galaxies, we use LENSTOOL to solve the lensing equation and produce a catalogue of lensed background galaxies. This catalogue contains the following information for each lensed object: the position, the shape parameters, and the redshift. Then this catalogue is processed through a numerical code that retrieves the input parameters of the lenses using a maximum-likelihood method as proposed by Schneider & Rix (1997) and as implemented by Natarajan & Kneib (1997). For each image ( $i$ ), given a mass model for the foreground lensing galaxies, we can compute the amplification matrix  $a_i$  as a sum of the contribution from all the foreground galaxies  $j$ ;  $z_j < z_i$  that lie within a circle of inner radius  $R_{min}$ , and outer radius  $R_{max}$  measured from the centre of the image ( $i$ ):

$$a_i = \sum_{\substack{z_j < z_i \\ d(i, j) < R_{max}}} a_{ij} \quad (32)$$

The total shear experienced by a background galaxy  $\gamma_i$  can be obtained by summing the contributions from all the foreground galaxies  $j$ ;  $z_j < z_i$  that lie within an annulus with inner and outer radii respectively at  $R_{min}$  and  $R_{max}$ .

Given the observed ellipticity  $\varepsilon_{obs}^i$  (defined as  $\varepsilon = (a - b)/(a + b)$ ) and the associated amplification matrix  $a_i$ , we are able to retrieve the intrinsic ellipticity  $\varepsilon_i^s$  of the source before lensing:

$$\varepsilon_i^s = F(\varepsilon_{obs}^i, a_i) \quad (33)$$

In the weak lensing regime, this relation can be simplified as:

$$\varepsilon_i^s = \varepsilon_{obs}^i + \gamma_i \quad (34)$$

In order to assign a likelihood to the parameters used to describe the lensing galaxies, we use  $P^s$ , the ellipticity probability distribution in the absence of lensing. Repeating this procedure for each image in the catalogue, we construct the likelihood function:

$$\mathcal{L} = \prod_i P^s(\varepsilon_i^s) \quad (35)$$

which is a function of the parameters used to define the mass models of the lenses. For each pair of chosen parameters, we can compute a likelihood function. The larger the likelihood function, the more accurate the retrieved parameters used to describe the lenses. The inversion from the observed ellipticity to the intrinsic ellipticity is fully analytic and takes into account all the non-linearities arising in the strong lensing regime, which may occur in the configuration with a cluster component.

The likelihood function for the parametric mass model for the lenses does have interesting convergence properties. The likelihood surface is topologically complex since the degeneracies in the problem tend to produce several maxima. However, the convergence in both the cluster lens case and field lens case is driven essentially by the width of the intrinsic ellipticity distribution of the sources. The degeneracies in this scheme are the generic ones that plague all lensing anal-

yses, the mass-sheet degeneracy (essentially the addition of a constant sheet of mass to the lens plane does not produce any discernable effect on the lensing of the background sources), the shot noise due to the finite number of sampled background sources and the details of the truncation of the mass profile of the lenses. The mass sheet degeneracy cannot be circumvented since we are necessarily measuring both the magnification  $\kappa$  and the shear  $\gamma$  from the same data points. Note that these are implicitly needed in computing the amplification matrix. Shot noise is more of a limitation in ground-based surveys when the number count of background galaxies is sparser compared to the space based data despite the fact that lensing helps by magnifying fainter sources that normally would not make it into a magnitude limited survey. The details of the mass profile, and in fact, the prescription used to truncate the mass at large radii influences the likelihood results. Since in galaxy-galaxy lensing (both in the field and interior to a cluster) we are most sensitive to the mass enclosed within an aperture and are less sensitive to the density profile in the inner regions the truncation of the mass distribution at large radii drives the convergence of the likelihood function. This can be clearly seen in the plots where the influence of  $R_{\max}$  shows up directly in the likelihood contours (see Fig. 5). Note that the parameters chosen to characterise the mass model: the central velocity dispersion and the truncation radius also contribute to the noise in the likelihood, thereby pointing to more efficient re-parameterisations that we also explore in the final section of this paper.

#### 4.2 Cluster weak lensing mass estimates

We construct a composite mass model for the cluster by superposing a large-scale smooth mass component and individual galaxies. As a first guess for the smooth mass model we use the averaged shear field obtained by simply binning up the shear in radial bins from the centre outward. This is a prior in the analysis that gets modified with every iteration once the clumps are added to the model. We simulate the deformations induced by a clump with known parameters (which can be easily derived from a weak lensing analysis for example). Then we add in the individual cluster galaxies and derive the shear of this composite system, which turns out to be larger than the shear for the clump alone as expected: this implies that we need to simultaneously modify the smooth component and the clumps during the optimisation process. In massive lensing clusters, about 10% of the total mass is associated with the individual galaxies (Natarajan 2002a). This large scale clump is described by a PIEMD profile with the following parameters:  $\sigma_0 = 1070 \text{ kms}^{-1}$ ,  $r_{\text{cut}} = 930 \text{ kpc}$  and  $r_{\text{core}} = 60 \text{ kpc}$ . This gives a total integrated mass of  $7.3 \cdot 10^{14} M_{\odot}$ . The mass we partition to galaxies is of the order of  $7.3 \cdot 10^{13} M_{\odot}$ . How do we modify the large-scale clump's parameters in order to match the shear field? We find that the velocity dispersion of the large-scale clump needs to be reduced by about 5%, keeping the others parameters fixed to accommodate the clumpiness.

## 5 RESULTS

We present the results obtained for the simulated data set, for the PIEMD, NFW and truncated power law (PL) models for two different configurations (Fig. 9, 10 and 11 at the end of the paper). The points mark the value of the INPUT parameters used in order to generate the simulated catalogue, and the cross stands for the value of the OUTPUT parameters as estimated from the maximum likelihood analysis. We will refer to the different plots by assigning them a number, the first one is the upper left plot, and the last one (plot number 9) is the lower right plot. The first plot shows the reference field situation: 25000 elliptical sources in a field of  $26 \times 26 \text{ arcmin}^2$ , which translates into a number density of about 35 galaxies per  $\text{arcmin}^2$ . Then the following plots (2, 3, 4) show the results obtained with 25000 circular sources, then with 40000 elliptical sources mimicking typical space observations with a density of 60 galaxies per  $\text{arcmin}^2$ , then with 12500 elliptical sources, corresponding to the ground based configuration with a galaxy density of 17 per  $\text{arcmin}^2$ , in a field configuration. Note that in the case of circular sources, we do not have to deal with the intrinsic ellipticity noise: the detection is therefore improved and the contours are tighter. The plots number 5 and 6 demonstrate the effect of the unknown redshift distribution for the background sources, in a field configuration. The last row represents the cluster configuration: the 'standard' configuration (plot 7), then configurations where an uncertainty on the cluster has been introduced (plot 8 and 9). For each plot, the contours represent the  $3\sigma, 4\sigma, 5\sigma$  confidence levels, and along the dotted lines, the mass within a projected radius  $R_{\text{aper}} = 100 \text{ kpc}$  is constant, equal to the value indicated on the plot.

### 5.1 The number of background lenses

For each profile, in the field configuration, we explore the influence of the background density on the detection. The 'standard' configuration has 25000 background sources (a density of 35 galaxies per  $\text{arcmin}^2$ ), we explore what happens when we increase this number to 40000 (60 per  $\text{arcmin}^2$ ), or reduce it to 12500 (17 per  $\text{arcmin}^2$ ). 17 galaxies per square arcminute corresponds to simulating ground based survey data, whereas 60 galaxies per square arcminute corresponds to the space based survey data. The main difference between the ground and space configurations is that from space, the statistics are significantly improved, and so the detection contours are significantly narrower.

### 5.2 The effect of assigning redshifts from an assumed distribution

To quantify the uncertainty arising from not knowing the redshifts for background sources, we performed the analysis after assigning redshifts drawn from a distribution. The 25000 sources are put at a mean redshift  $z_s$  and images are simulated. When constructing the simulated catalogue, the background objects are assigned a mean redshift of  $z_s + \delta_z$ . This catalogue is then input into the maximum likelihood code. Since the strength of the shear is proportional to the distance between the sources and the lenses, under estimating the source redshifts leads to an overestimate of the lens



$\delta z_S$ (%)	$\delta E$	$\delta\sigma_0$	$\sigma_0$
0	0	0	[174-196]
20	0.05	-7	[170-190]
-20	-0.05	7	[180-208]

**Table 1.** Influence of an uncertainty in the mean redshift of the sources: an error of  $\delta z_S$  correspond to a variation of  $E(z_L, z_S)$  equal to  $\delta E$ , which correspond to a variation on  $\sigma_0$  of order  $\delta\sigma_0$ . We see from this table that this estimated variation on  $\sigma_0$  is coherent with the variation in the detection range as derived from the maximum likelihood analysis.

masses and tends to shift the confidence contours toward higher values for the velocity dispersion. For the same reason, systematically overestimating the source redshifts leads to an underestimate of the galaxy masses. In any case, we find that a redshift uncertainty of  $\pm 0.2$  does not dramatically modify the conclusions. This is typically the precision we can get with photometric redshift estimation which is encouraging for future surveys. This results is coherent with a recent study by Kleinheinrich et al., 2004 based on the galaxy-galaxy lensing results from the COMBO-17 survey. They found that it is of great importance to know the redshifts of individual lens galaxies in order to constrain the properties of their dark matter halos, but that the knowledge of individual source redshifts improves the measurements only very little over use of statistical source redshift distribution.

To be more quantitative, let us consider the lensing equation and express it for a constant deflection angle. For a PIEMD profile with a given  $\sigma_0$ , we have:

$$\sigma_0^2 \frac{D_{LS}}{D_S} = \text{constant}; \quad \text{and} \quad \frac{D_{LS}}{D_S} = E(z_l, z_s) \quad (36)$$

as introduced in Golse (2002). Therefore the equation can be rewritten as:

$$\sigma_0^2 E(z_L, z_S) = \text{constant} \quad (37)$$

The lenses are kept at a redshift of 0.2, and the mean redshift of the sources is changed by  $\delta z = \pm 20$  %. We then evaluate the corresponding  $\delta\sigma_0$  error introduced in the retrieval of the central velocity dispersion in the likelihood analysis. Table 1 gives the results: when we put an error of  $\delta z_S$  (%), this give a variation of  $E(z_L, z_S)$  equal to  $\delta E$ , and the corresponding variation on  $\sigma_0$  is of order  $\delta\sigma_0$ . This range of values is given by the projection of the  $3\sigma$  contours along the  $\sigma_0$  axis. We can see that the variation in the detection range is in agreement with the calculations made.

### 5.3 Influence of the uncertainty in the cluster modeling

When working with the real data, we will have to put in by hand the description of the cluster. The reliability of the results will depend on the accuracy with which we describe cluster. In order to study the influence of the uncertainty of the cluster profile, the cluster component is described by a PIEMD profile with a velocity dispersion of  $\sigma_{cluster} = 1000 \text{ kms}^{-1}$ . When constructing the simulated

catalogue, the cluster component is assigned a velocity dispersion of  $\sigma_{cluster} + \delta\sigma$ . The likelihood is then computed for this case.

## 6 DISCUSSION AND CONCLUSIONS

### 6.1 Constraints obtained on mass profiles

For the PIEMD and NFW profiles, we found that we are able to retrieve the characteristic halo parameters with extremely good accuracy, for every configuration. In fact, interestingly enough, the dotted lines in Figs. 9, 10, and 11 show us that the aperture mass is retrieved very accurately. This immediately suggests the re-parameterisation of models considered here: rather than fitting in the  $(\sigma_0, r)$  plane, we can fit the deformations directly in the  $(M_{aper}, R_{aper})$  plane. This formulation is explored in the next section.

For the PL profile, we find that we can put some constraints on  $\alpha$ , the slope of the density profile, but not on the velocity dispersion, since the likelihood function does not always converge along that direction. So we can use this profile to estimate the slope of dark matter halos, without trusting the constraints we get on the velocity dispersion for the profile.

### 6.2 Influence of $R_{max}$

When working with real data, the results we get depend on the value chosen for  $R_{max}$ . When we take a low value for  $R_{max}$ , the shear for the image (i) is calculated with fewer lenses, and we find that the contours do not close in  $r_{cut}$ . When the value of this parameter is increased, the contours converge and close. On the other hand, picking a high value for  $R_{max}$  introduces some noise in calculating the shear, and can dilute the galaxy-galaxy lensing signal significantly: lenses that do not *effectively* participate in the lensing of an image if utilised in the calculation become a source of noise. Fig. 5 illustrates precisely this situation: for a given value of  $R_{max}$ , we obtain a good estimate of  $\sigma_0$ , but the robustness of the constraint on  $r_{cut}$  is directly related to the value of  $R_{max}$ . Others authors have reported that their results are sensitive to the value of this parameter (*e.g.* Kleinheinrich, PhD thesis).

The choice of  $R_{max}$  is therefore important. To get the order of magnitude of this parameter, we compare the characteristic noise in the problem, *i.e.*  $\frac{0.25}{\sqrt{N}}$ , to the signal we are sensitive to *i.e.* the reduced shear - the factor of 0.25 is the width of the intrinsic ellipticity distribution and  $N$  is the number of background objects at a distance  $r$  from a lensing galaxy. This noise has been estimated by analysing data from the ground-based CFH12k observations of the cluster A1763 at a redshift of  $z = 0.22$ . From space, we expect the number of background objects to be about 6/7 times higher. Fig. 6 shows that a value of about 100" can be used for  $R_{max}$ .

On the other hand, the choice of the parameter  $R_{min}$  does not influence the results, so we fix this parameter to be of the order of a few kpc.

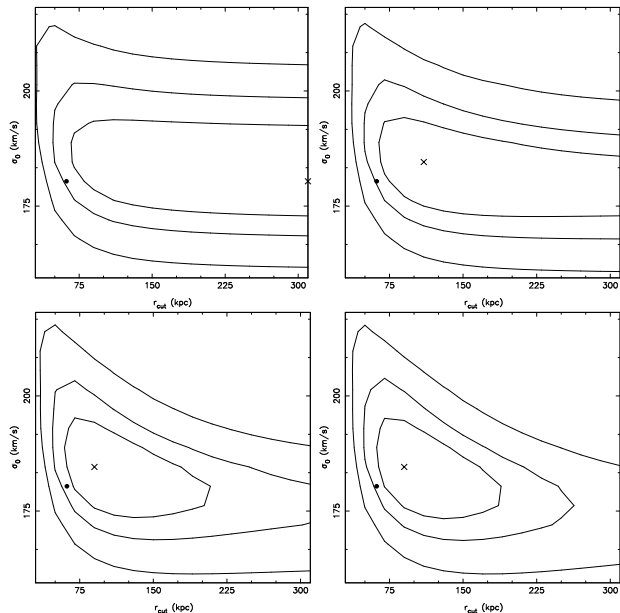


**Figure 5.** The PIEMD profile, in a field configuration: In the panels from left to right, the value of  $R_{max}$  increases from  $30''$ ,  $60''$ ,  $90''$  to  $150''$ . When  $R_{max} > 100''$ , the contours cover along the  $r_{cut}$  axis. Note that the convention throughout this work is that the dot marks the value of the input parameters and the cross marks the retrieved output values.

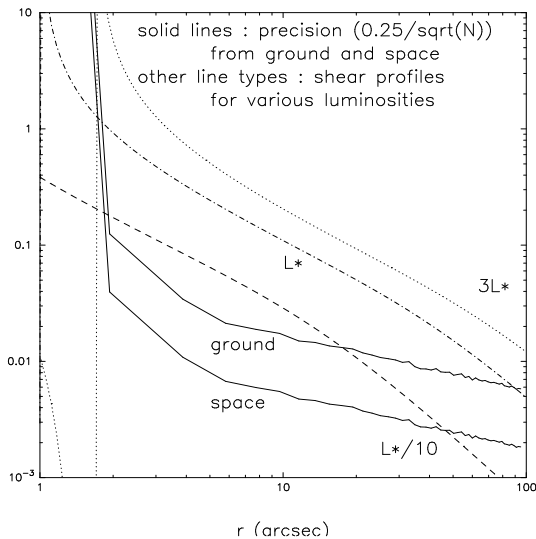


**Figure 6.** Comparing the signal to noise for an estimate of the optimal choice for  $R_{max}$ . The solid lines correspond to the characteristic ellipticity (due to the width of the ellipticity distribution),  $\frac{0.25}{\sqrt{N}}$  as a function of radius, from ground and space. The other line types (dot, dashed and dot-dashed) correspond to the signal-to-noise reduced shear as a function of radius for typical luminosities.

## 7 RE-PARAMETERIZATION OF THE PROBLEM

Thus far, we have performed the likelihood analysis to optimize the values of two parameters  $\sigma_0$  and  $r_{cut}$  (or  $r_s$ ). A different set of parameters can be chosen for maximizing the

likelihood, for instance  $M_{aper}$  and  $R_{aper}$ , which we explore below.

We have:

$$\mathcal{L} = \mathcal{L}(\sigma_0, r_{cut}) \quad \& \quad M_{aper} = M_{aper}(R_{aper}, \sigma_0, r_{cut}) \quad (38)$$

so we can write:

$$\sigma_0 = \sigma_0(M_{aper}, R_{aper}, r_{cut}) \quad (39)$$

the likelihood function then becomes:

$$\mathcal{L}(M_{aper}, R_{aper}, r_{cut}) \quad (40)$$

and by summing over  $r_{cut}$ , we get:

$$\mathcal{L}' = \sum_{r_{cut}} \mathcal{L}(M_{aper}, R_{aper}, r_{cut}) \quad (41)$$

$$\mathcal{L}' = \mathcal{L}'(M_{aper}, R_{aper}) \quad (42)$$

The sum is performed for a set of  $r_{cut}$  values around the input value used to simulate the catalogue and the range defined by the projection of the  $3\sigma$  contour level along the  $r_{cut}$  axis. The results do not depend strongly on the range used to do the sum. Fig. 7 and 8 shows the  $\mathcal{L}'$  contours we get for the NFW and the PIEMD profiles. Since the PL profile does not have a cut-off radius we cannot compare it easily with the re-parameterized PIEMD and NFW profiles. The plots above show that we can put strong constraints on the aperture mass, the crossed line represents the line  $M_{aper}(R_{aper})$  as computed with the input model used to generate the simulated catalogue.

The motivation of such a re-parameterisation is that we deal with more direct physical quantities than halo parameters, that is an aperture mass calculated within an aperture radius. The primary motivation for galaxy-galaxy lensing studies was to measure halo masses, so this offers a more convenient parameterisation for that purpose. This is also a different way of measuring masses compared to the aperture densitometry method. Moreover, it is more suited to the case of clustered galaxies since we are not able to integrate the shear profile for any individual galaxy.

To conclude in this paper, we have discussed galaxy-galaxy lensing in the context of measuring masses of field and cluster galaxies. We compare the robustness of recovering input parameters for the mass distribution of lenses from a ground based survey and space based observations. We explore a wide range of input mass models for galaxy halos. We simulate the galaxy-galaxy lensing effect and generate synthetic catalogues. A maximum likelihood method is applied to the catalogues to successfully recover the lens parameters in various configurations. Going beyond the standard parameterisation of a dark matter halo, we propose a re-parameterisation of the problem in terms of more direct physical quantities: the aperture mass calculated within an aperture radius. The main result of this re-parameterisation is that we are able to put even stronger constraints on the aperture mass for an  $L^*$  galaxy.

## ACKNOWLEDGEMENTS

ML thanks the Astrophysics Department of the Pontificia Universidad Católica, Santiago, Chile for their hospitality, where a significant portion of this work was completed.

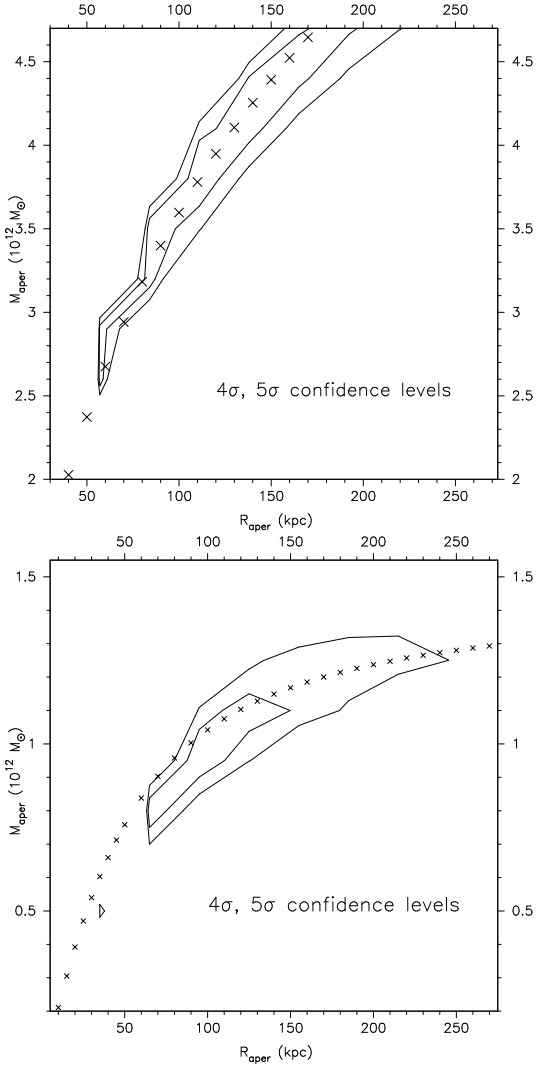


**Figure 7.** The likelihood  $\mathcal{L}'(M_{aper}, R_{aper})$  for the NFW (upper panel) and the PIEMD profile (lower panel). The crossed line represents the  $M_{aper}(R_{aper})$  contour obtained with the input parameters used to describe the foreground lenses in the **cluster** configuration.

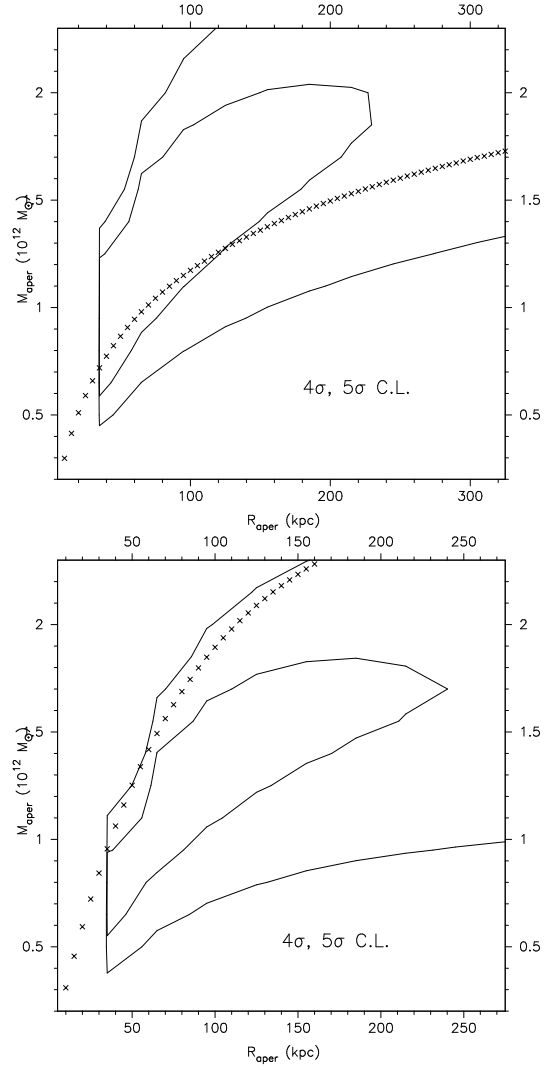


**Figure 8.** The likelihood  $\mathcal{L}'(M_{aper}, R_{aper})$  for the NFW (upper panel) and the PIEMD profile (lower panel). The crossed line represents the  $M_{aper}(R_{aper})$  contour obtained with the input parameters used to describe the foreground lenses in the **field** configuration.

## REFERENCES

- Bardeau, S., Kneib J-P., Czoske, O., Richard, J., Soucail, G., Smail, I., & Ebeling, H., 2004, In preparation.
- Bartelmann, M., 1996, *A&A*, 313, 697-702.
- Brainerd T.G, Blandford R.& Smail I., 1996, *ApJ*, 466: 623-637.
- Brainerd T.G. & Specian M.A., 2003, *ApJ*, 593:L7-L10.
- Davis, M et al., 2003, *Proceedings of the SPIE*, Volume 4834, page 161-172.
- Fassnacht, C. D., et al., 1999, *ApJ*, 117, 658.
- Fisher P. et al., 2000: *ApJ*, 120: 1198.
- Gavazzi R., Fort B., Mellier Y., Pellò R.& Dantel-Fort M., 2003, *A&A*, 403:11-27.
- Geiger, B., & Schneider, P., 1998, *MNRAS*, 295, 497.
- Golse, G., 2002, PhD thesis, Université Paul Sabatier.
- Griffiths R.E., Casertano S., Im M.& Ratnatunga K.U., 1996, *MNRAS*, 282, 1159-1164.
- Hjorth Jens & Kneib Jean-Paul, 2002, submitted to *ApJ*.
- Hoekstra H. et al., 2003, *MNRAS*, 340, 609-622.
- Hoekstra H., Yee, H. K. C., & Gladders, M., 2004, *ApJ*, 606, 67.
- Kaiser, N., Squires, G. & Broadhurst, T., 1995, *ApJ*, 449:460-475.
- Keeton C.R., Kochanek, C.S., & Seljak, U., 1997, *ApJ*, 482,604.
- Kleinheinrich M., 2004, *A&A*, submitted (astro-ph/0404527).
- Kneib, J-P., 1993, PhD thesis, Université Paul Sabatier.
- Kneib J., Cohen J. G., Hjorth J., 2000, *ApJ*, 544, L35
- Kneib, J-P, Ellis R.S., Smail, I., Couch W.J., Sharples R.M., 1996, *ApJ*, 471:643-656.
- Kneib J.P., Hudelot P., Ellis R., Treu T., Smith G., Marshall P., Czoske O., Smail I. & Natarajan P., 2003, *ApJ*, 598:804-817.
- Koopmans L.V.E. & Treu T., 2003, *ApJ*, 583:606-615.
- Le Fevre O. et al., 2003, *Proceedings of the SPIE*, Volume 4834, page 173-182.
- McKay T.A. et al., 2001, *ApJ*, submitted (astro-ph/0108013).
- Möller, O., Natarajan, P., Kneib, J.-P. & Blain A.W., 2002, *ApJ*, 573:562-575.
- Natarajan, P., & Kneib, J-P., 1997, *MNRAS*, 287, 833.
- Natarajan, P., Kneib, J-P., Smail, I., and Ellis, R., 1998, *ApJ*, 499:600-607.
- Natarajan, P., Kneib, J-P., & Smail, I., 2002, *ApJ*, 580:L11-L15.
- Natarajan, P., Loeb, A., Kneib, J-P., & Smail, I., 2002, *ApJ*, 580:L17-L20.
- Navarro, J., Frenk, C. S., & White, S. D. M., 1997, *ApJ*, 462, 563.
- Prada F., Vitvitska M., Klypin A., Holtzman J.A., Schlegel D.J., Grebel E.K., Rix H.W., Brinkmann J., McKay T.A. & Csabai I., 2003, *ApJ*, 598:260-271.
- Phillips P. M., et al., 2000, *MNRAS*, 319, L7.
- Refregier, A., 2003, *ARA&A*, 41:645-668.
- Rhodes J. et al. (SNAP collaboration), 2003, *Astroparticle Physics*, Volume 20, Issue 4, Pages 377-389.
- Schneider P., Ehlers J., Falco E. E., 1992, *Gravitationnal Lenses*. Springer, New York.
- Schneider P. & Rix H.W., 1997, *ApJ*, 474: 25-36.
- Sheldon, E.S., Frieman, J., Johnston, D., Mckay, T., & SDSS Collaboration 2003, American Astronomical Society Meeting, 202.
- Treu T.& Koopmans L.V.E., 2004, Submitted to *ApJ*.

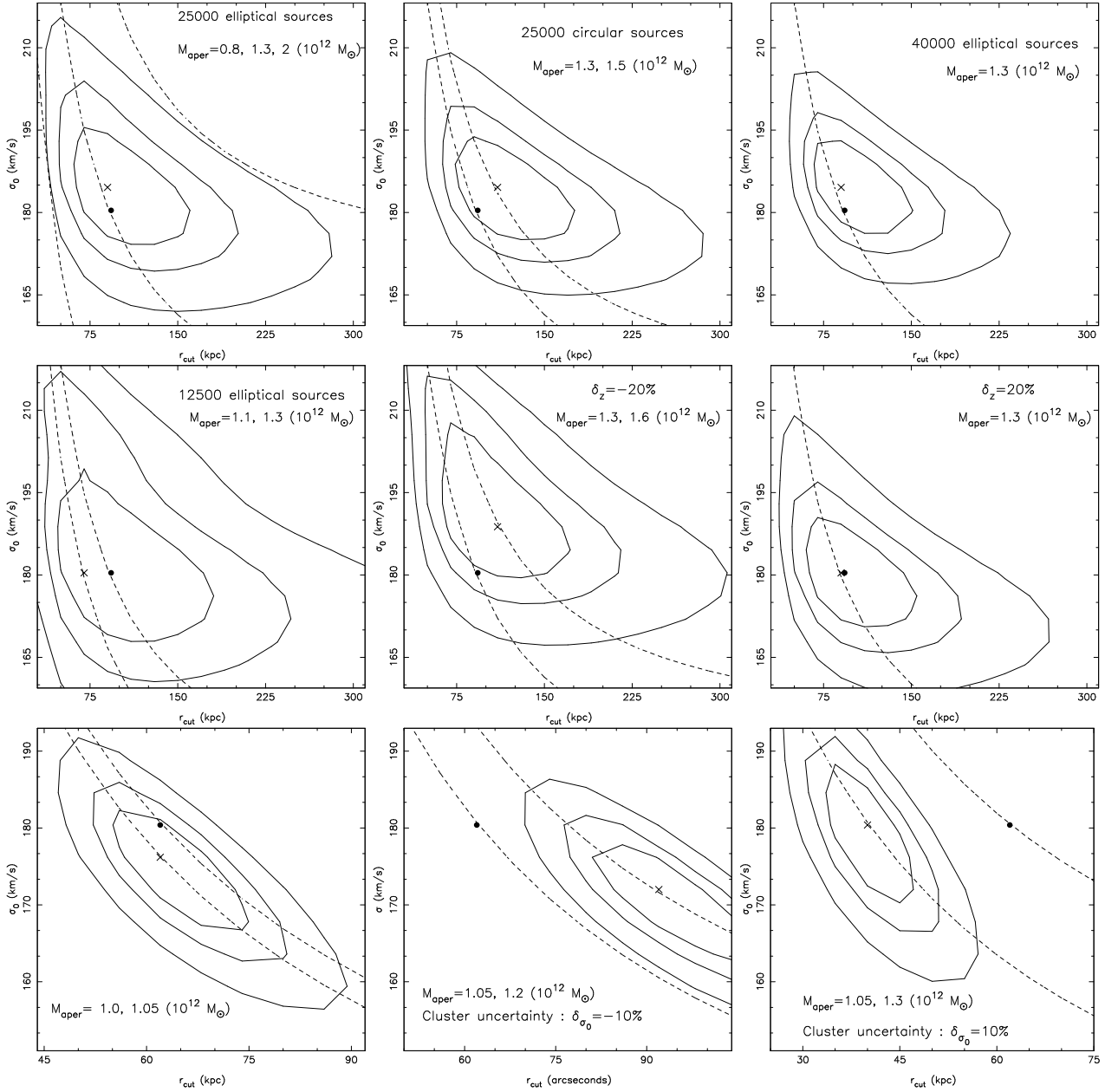


**Figure 9.** Results for the PIEMD profile. The top left plot (number 1) is the reference field situation with 25,000 elliptical background sources in a field of  $26 \times 26$  arcmin<sup>2</sup>, corresponding to a density of background sources equal to about 35 galaxies per arcmin<sup>2</sup>. Then the following plots (2, 3, 4) show the results obtained with 25,000 *circular* sources, then with 40,000 elliptical sources mimicking typical space observations with roughly 60 galaxies per arcmin<sup>2</sup>, then with 12,500 elliptical sources, corresponding to the ground based configuration with a galaxy number density of 17 galaxies per arcmin<sup>2</sup>. The plots number 5 and 6 show the effect of introducing an uncertainty in the mean redshift of the source population: this uncertainty is equal to -20% (left) and +20% (right). The last row show the results from the cluster configuration: the reference cluster configuration (plot 7), then configurations where an uncertainty on the cluster modeling is introduced: knowing the central velocity dispersion of the cluster to within  $\pm 10\%$ . The contours in this figure represent the  $3\sigma, 4\sigma, 5\sigma$  confidence levels, and along the dotted lines in every panel, the mass within a projected radius  $R_{aper}$  of 100 kpc is kept constant at the value indicated on the plot. Note that the dot indicates input values and the cross the retrieved output.

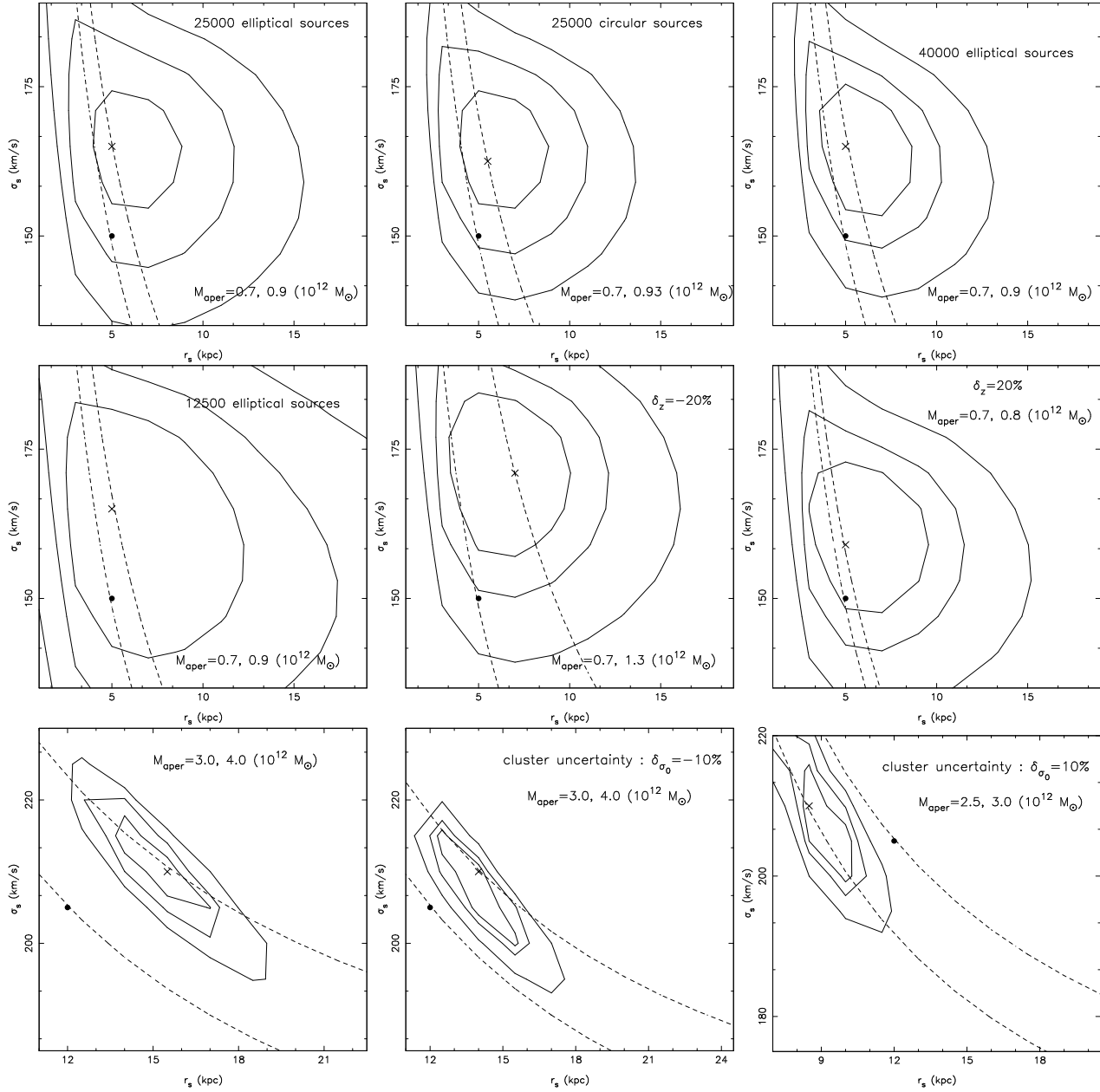


**Figure 10.** Results from the NFW profile: the top left plot (number 1) is the reference field situation with 25,000 elliptical background sources in a field of  $26 \times 26$  arcmin<sup>2</sup>, corresponding to a density of background sources equal to about 35 galaxies per arcmin<sup>2</sup>. The following plots (2, 3, 4) show the results obtained with 25,000 *circular* sources, then with 40,000 elliptical sources, corresponding to data obtained from space with 60 galaxies per arcmin<sup>2</sup>, then with 12,500 elliptical sources, corresponding to the ground-based data of about 17 galaxies per arcmin<sup>2</sup>. The plots number 5 and 6 show the effect of introducing an uncertainty in the mean redshift of the source population: this uncertainty is equal to -20% (left) and +20% (right). The last row show the results from the cluster configuration: the reference cluster configuration (plot 7), the effect of introducing an uncertainty of  $\pm 10\%$  in the central velocity dispersion of the cluster model used. Contours in these figures represent the  $3\sigma$ ,  $4\sigma$ , and  $5\sigma$  confidence levels, and along the dotted lines in each panel, the mass within a projected radius  $R_{\text{aper}}$  of 100 kpc is kept constant, with  $M_{\text{aper}}$  at the quoted value indicated on the plot. Note that the dot indicates input values and the cross the retrieved output.

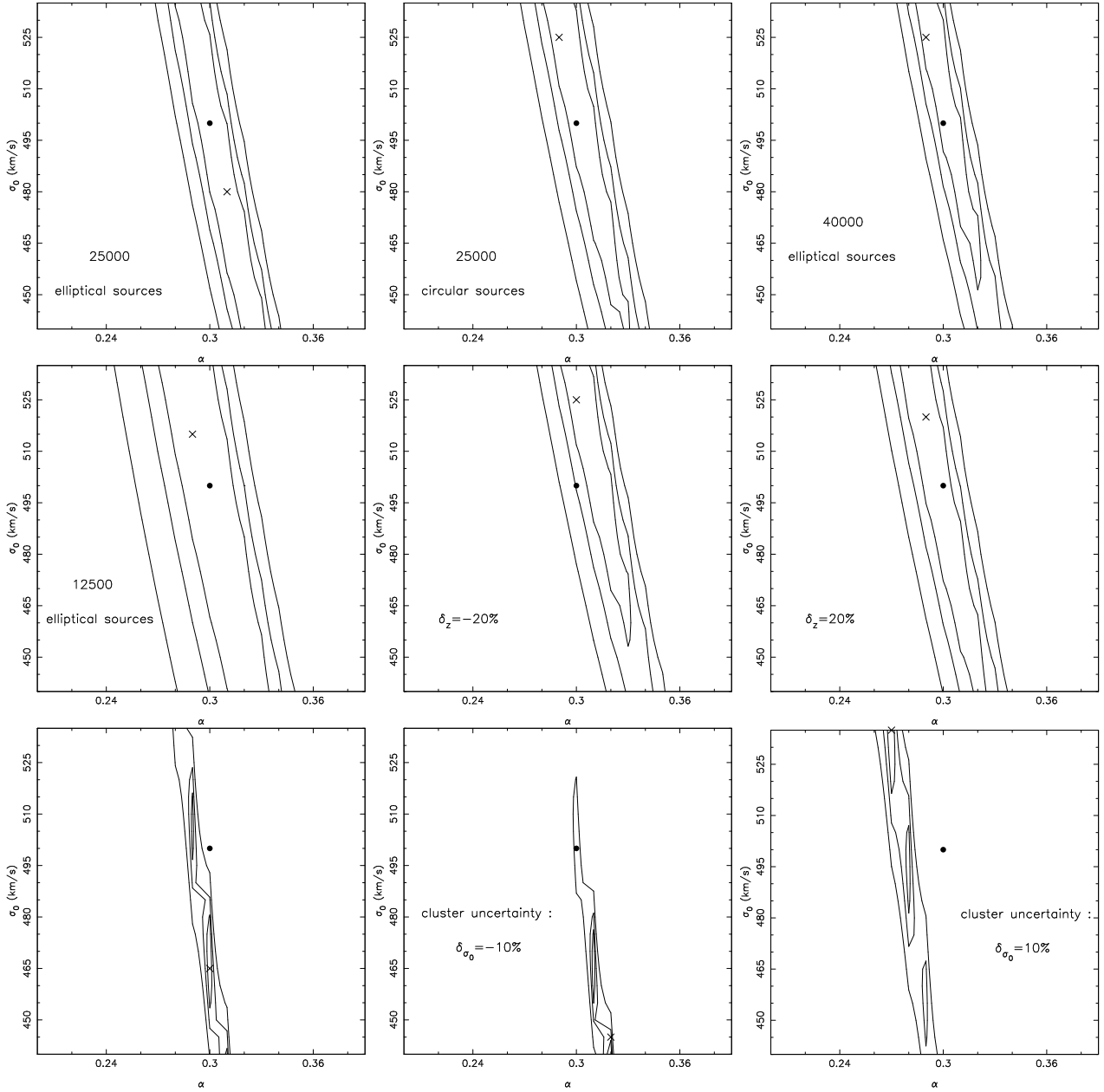


**Figure 11.** Results from the PL profile. The top left plot (number 1) is the reference field situation with 25,000 elliptical background sources in a field of  $26 \times 26$  arcmin<sup>2</sup>, corresponding to a density of background sources equal to about 35 galaxies per arcmin<sup>2</sup>. Then the following plots (2, 3, 4) show the results obtained with 25,000 *circular* sources, then with 40,000 elliptical sources corresponding to a typical space based observation yielding 60 galaxies per arcmin<sup>2</sup>, then with 12,500 elliptical sources corresponding to ground based data with a galaxy number density of about 17 galaxies per arcmin<sup>2</sup>. The plot number 5 and 6 show the effect of introducing an uncertainty in the mean redshift of the source population: this uncertainty is equal to -20% (left) and +20% (right). The last row show the results from the cluster configuration: the reference cluster configuration (plot 7), and then configurations where uncertainty has been introduced in the cluster modeling. The contours in all these panels represent the  $3\sigma$ ,  $4\sigma$  and  $5\sigma$  confidence levels. Note that the dot indicates input values and the cross the retrieved output.